A GALERKIN-CHARACTERISTIC METHOD FOR LARGE-EDDY SIMULATION OF TURBULENT FLOW AND HEAT TRANSFER[*]

MOFDI EL-AMRANI[†] AND MOHAMMED SEAID[‡]

Abstract. This work aims at the development of a nonoscillatory Galerkin-characteristic method for large-eddy simulation of turbulent flow and heat transfer. The method is based on combining the modified method of characteristics with a Galerkin finite element discretization of the incompressible Navier–Stokes/Boussinesq equations in primitive variables. It can be interpreted as a fractional step technique where the convective part and the Stokes/Boussinesq part are treated separately. A limiting procedure is implemented for the reconstruction of numerical solutions at the departure points. The main feature of the proposed Galerkin-characteristic method is that, due to the Lagrangian treatment of convection, the standard Courant–Friedrichs–Levy condition is relaxed, and the time truncation errors are reduced in the Stokes/Boussinesq part. To solve the generalized Stokes/Boussinesq problem we implement a conjugate gradient algorithm. This method avoids projection techniques and does not require any special correction for the pressure. We verify the method for an advection-diffusion equation with a known analytical solution and for the benchmark problem of mixed convection flow in a squared cavity. We also present numerical results for a problem of heat transport in the Strait of Gibraltar. The Galerkin-characteristic method has been found to be feasible and satisfactory.

Key words. Galerkin-characteristic method, large-eddy simulation, heat transfer, finite element method, mixed convection, sea-surface temperature

AMS subject classifications. 76F35, 74S05, 65M25

DOI. 10.1137/080720711

1. Introduction. The large-eddy simulation (LES) equations for incompressible thermal flows are obtained by applying a spatial filtering to the Navier–Stokes equations subject to the Boussinesq approximation; see [5, 4, 17, 23, 16, 12] and the references therein. However, this procedure introduces a term called a subgrid stress tensor which needs to be modelled. This term has to be seen as the interaction between the large and small scales in the system. In the current study, we will concentrate on a subgrid problem based on the Smagorinsky model [27]. The LES is normally performed on grids that are just fine enough to resolve the large flow scales, and numerical errors on such grids can have large effects on the simulation results. Although in the literature (see [12] and references therein) many numerical schemes have been presented, it is still not clear what the effect of the numerical and modelling errors in the LES is. However, it is commonly known that implicit time-stepping schemes are important in LES because they offer a mean to obtain accurate solutions with larger time steps that may be required for explicit methods. It is well-established that the numerical treatment of the LES equations often present difficulties due to their nonlinear form, incompressibility condition, the presence of the convective term, coupling between the energy equation, and the equations governing the fluid motion. In the LES problems, convective terms are distinctly more important than the diffusive terms; particularly when the Reynolds numbers reach high values, these convective terms are a source of computational difficulties and nonphysical oscillations.

[†]Departamento de Matemática Aplicada, Universidad Rey Juan Carlos, 28933 Móstoles-Madrid, Spain (mofdi.elamrani@urjc.es).

[‡]School of Engineering, University of Durham, South Road, Durham DH1 3LE, UK (m.seaid@durham.ac.uk).

The Galerkin-characteristic (known also by semi-Lagrangian) methods have been largely studied and have proved their efficiency for convection-dominated flow problems. The central idea in these methods is to rewrite the governing equations in terms of Lagrangian coordinates as defined by the particle trajectories (or characteristics) associated with the problem under consideration. The time derivative and the advection terms are combined as a directional derivative along the characteristics, leading to a characteristic time-stepping procedure. Consequently, these methods are known to be unconditionally stable, independent of the diffusion coefficient, and optimally accurate at least when the inner products in the Galerkin procedure are calculated exactly. A Galerkin-characteristic has been investigated in references [6, 21, 29], among others. In [21], a first-order Galerkin-characteristic method combined with a finite element method has been analyzed for the Navier–Stokes equations. It has been shown that the method is unconditionally stable provided the characteristics are transported by the divergence-free field that is deduced from the flow velocity. The case where the characteristics are transported by a discrete velocity field which is not divergence-free has been studied in [29]. An analysis of a Galerkin-characteristic method using finite difference discretization has been treated in [6] for convection-diffusion equations. In all of these references the convergence and stability of the method are proven under the assumption that all of the inner products are calculated exactly. Furthermore, the evaluation of the fluid particles at the departure points in [6, 21, 29] is performed using an L^2-projection on the finite element space. In many applications, the evaluation of integrals in the L^2-projection is the most difficult part of these approaches. For the Galerkin-characteristic method proposed in the current work, the solutions at characteristic feet are approximated by interpolation from finite element basis functions. An advantage of combining the finite element method with the Galerkin-characteristic method is that interpolation procedures at the characteristic feet can be performed using the finite element basis functions. Obviously, this reduces the computational cost and requires less implementation work than using the L^2-projection on the corresponding finite element spaces. Furthermore, the method is suitable for complex geometries, independent of the sizes and arrangement of the mesh elements, and can easily combine different polynomial orders of elements. These properties are very useful when coupling the LES equations to complex components to simulate applications, for instance, in multiphase flows and transport in porous media.

In LES problems, the convection process is repeated continuously. Thus, some artifacts which can be tolerated for one step might become a serious issue as the errors start building up after several steps. For this reason, in most Galerkin-characteristic methods linear interpolation procedures result in an oscillation-free solutions. However, applied to LES equations a Galerkin-characteristic method would require higher interpolation for higher accuracy. The main problem with the high-order interpolation procedures is that high-degree polynomials they use might show oscillatory behavior as they are forced to satisfy the continuity condition at the nodal points. In order to avoid the principal drawback of the conventional Galerkin-characteristic methods, that is, the failure to preserve monotonicity, we incorporate limiters into our algorithm to convert the method to nonoscillatory and shape preserving at minor additional computational cost. The procedure consists of writing the local solution as a convex combination of a high-order and low-order interpolant solutions in the host element where the characteristic foot is localized. These solutions use two different basis functions of high-order and low-order, respectively. This adjustment procedure removes the oscillations as it stabilizes the system towards a monotone solution. The method uses ideas of the flux-corrected transport algorithm [32]. A rigorous error

analysis of this nonoscillatory Galerkin-characteristic method was performed in [9] for the incompressible Navier–Stokes equations. In addition, numerical results and comparisons between this method and the conventional modified method of characteristics are shown in [26, 25] for finite difference discretization and in [24] for finite element discretization. It should be stressed that a similar Galerkin-characteristic method has been successfully implemented by the authors for solving laminar incompressible viscous flows in [10, 7, 11].

This paper is devoted to investigating the performance of the nonoscillatory Galerkin-characteristic method for the LES of turbulent flow and heat transfer. The application of this method has been demonstrated using the standard benchmark problem of mixed convection in a squared cavity and a problem of forced convection flow and heat transport in the Strait of Gibraltar. Some results are presented as validation examples, and others, to the best of our knowledge, are reported for the first time. Numerical results presented in this study show that an interesting feature of the nonoscillatory Galerkin-characteristic method is to allow large time steps without deteriorating accuracy of the computed solutions.

The present paper is organized as follows. The description of the model employed is presented in section 2. Section 3 is devoted to the formulation of the Galerkin-characteristic method. This section includes an adjusted characteristics method for the convection fractional stage and a conjugate gradient algorithm for the Stokes/Boussinesq stage. In section 4, we present numerical results and examples for LES of turbulent flow and heat transfer. Our new approach is shown to enjoy the expected accuracy as well as the robustness. Some concluding remarks are given in section 5.

2. Equations of turbulent flow and heat transfer. The description of the evolution of a fluid in terms of velocity, the density and the temperature has proven to be very successful. Obviously, this description cannot be valid for very small scales at which the molecular nature of the medium has to be taken into account. In the present work we consider the LES to model these small scales and also to analyze the subgrid errors. The basic idea of LES is to compute a space-averaged flow field accurately. To achieve this, each flow variable ω is decomposed into a large-scale component $\overline{\omega}$ and a subgrid scale component ω'. The large-scale component is obtained by an application of a filter operator. In practice, this operator is a convolution integral of the form

$$\overline{\omega}(\mathbf{x}, t) = \int_{\mathbb{R}^2} G_\Delta \left(|\mathbf{x} - \mathbf{y}| \right) \omega(\mathbf{y}, t) \, d\mathbf{y},$$

where $\mathbf{x} = (x, y)^T$ is the space coordinate, t denotes the time, and G_Δ is the filter such as volume-average box-filter; see for example [23].

The governing equations for flow and heat transport are the equations of mass, momentum, and energy for a viscous Newtonian fluid subject to the Boussinesq approximation. Here, the Newtonian assumption guarantees a linear dependence between the shear stress and the velocity gradient, while the Boussinesq approximation ensures that the density differences are confined to the buoyancy force without violating the incompressibility condition. Hence, the filtered governing Navier–Stokes/Boussinesq equations are expressed in vector form as

$$\nabla \cdot \mathbf{u} = 0,$$

$$(2.1) \qquad \rho_\infty \left(\frac{\partial \mathbf{u}}{\partial t} + \mathbf{u} \cdot \nabla \mathbf{u} \right) + \nabla p = \nabla \cdot \left(2\mu \mathbf{S}(\mathbf{u}) \right) - \nabla \cdot \mathcal{T}(\mathbf{u}) + \mathbf{F},$$

$$\rho_\infty c_p \left(\frac{\partial T}{\partial t} + \mathbf{u} \cdot \nabla T \right) = \nabla \cdot (\kappa \nabla T) - \nabla \cdot \mathcal{H}(T),$$

where the "overbar," used to refer to filtered variables, has been omitted for ease in notation. Here, $\mathbf{u} = (u, v)^T$ is the velocity field, p the pressure, T the temperature, ρ_∞ the reference density, μ the viscosity, c_p the specific heat at constant pressure, and κ the thermal diffusivity coefficient. In (2.1),

$$(2.2) \qquad \mathbf{S}(\mathbf{u}) = \frac{1}{2}\left(\nabla\mathbf{u} + \nabla\mathbf{u}^T\right)$$

is the strain-rate tensor, and the force term $\mathbf{F}$ due to the Boussinesq approximation is defined as

$$\mathbf{F} = \rho_\infty\left(1 - \beta(T - T_\infty)\right)\mathbf{g},$$

with $\mathbf{g}$ is the gravity force, T_∞ a temperature reference, and β the coefficient of thermal expansion. The Reynolds subgrid-scale tensor $\mathcal{T}(\mathbf{u})$ and the heat subgrid-scale term $\mathcal{H}(T)$ are

$$\mathcal{T}(\mathbf{u}) = \overline{\mathbf{u}\otimes\mathbf{u}^T} - \mathbf{u}\otimes\mathbf{u}^T, \qquad \mathcal{H}(T) = \overline{\mathbf{u}T} - \mathbf{u}T.$$

To model these subgrid-scales in terms of filtered velocity field $\mathbf{u}$ and filtered temperature T, we use the Smagorinsky model [27] i.e.,

$$(2.3) \qquad \mathcal{T}(\mathbf{u}) \approx -\mu_t\mathbf{S}(\mathbf{u}), \qquad \mathcal{H}(T) \approx -\kappa_t\nabla T.$$

The turbulent viscosity μ_t and the turbulent thermal diffusivity κ_t are

$$(2.4) \qquad \mu_t = (c_s\,\Delta)^2\,\|\mathbf{S}(\mathbf{u})\|, \qquad \kappa_t = \frac{\mu_t}{\sigma_T},$$

where

$$(2.5) \qquad \|\mathbf{S}(\mathbf{u})\| = \left(\mathbf{S}(\mathbf{u}){:}\mathbf{S}(\mathbf{u})\right)^{\frac{1}{2}},$$

and c_s is a model constant which has to be chosen a priori, Δ is the grid filter width taken to be proportional to the grid size h, and σ_T is the turbulent Prandtl number set to 0.9 in our LES results. Substituting (2.3) into (2.1) we obtain

$$(2.6) \qquad \begin{aligned} \nabla\cdot\mathbf{u} &= 0, \\ \rho_\infty\frac{D\mathbf{u}}{Dt} + \nabla p &= \nabla\cdot\left((2\mu + \mu_t)\,\mathbf{S}(\mathbf{u})\right) + \mathbf{F}, \\ \rho_\infty c_p\frac{DT}{Dt} &= \nabla\cdot\left((\kappa + \kappa_t)\,\nabla T\right), \end{aligned}$$

where $\frac{D\omega}{Dt}$ is the material derivative of any flow variable ω defined by

$$(2.7) \qquad \frac{D\omega}{Dt} = \frac{\partial\omega}{\partial t} + \mathbf{u}\cdot\nabla\omega.$$

Notice that $\frac{D\omega}{Dt}$ measures the rate of change of the function ω following the trajectories of the flow particles. The main idea behind the Galerkin-characteristic method is to impose a regular grid at the new time level and to backtrack the flow trajectories to the previous time level. At the old time level, the quantities that are needed are evaluated by interpolation from their known values on a regular grid.

The LES equations (2.6) have to be solved for a fixed time interval in a bounded space domain Ω. Boundary and initial conditions have to be inserted in equations (2.6) to provide a well-posed mathematical problem. These conditions strongly depend on the problem under consideration, and their discussion is postponed for section 4 where numerical examples are presented.
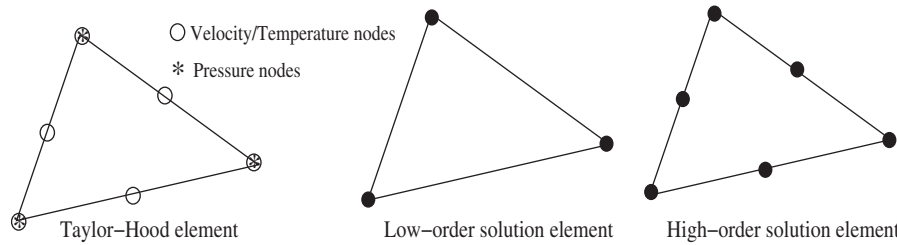
FIG. 3.1. *Taylor–Hood element, low-order and high-order finite elements used in the simulations.*

3. The Galerkin-characteristic method. The spatial discretization of (2.6) is performed using the finite element discretization. Thus, we cover the space domain Ω, with a quasi-uniform partition Ω_h of small elements $\mathcal{K}_j$ such that $\Omega = \bigcup_{j=1}^{Ne} \mathcal{K}_j$, where Ne is the number of elements in Ω_h. In the present study, the conforming finite element spaces for velocity/temperature and pressure that we use are Taylor–Hood finite elements P_2/P_1 (see the left plot in Figure 3.1), i.e., polynomial of second degree for the velocity/temperature and polynomial of first degree for the pressure, respectively. It is known that for such elements the discrete velocity/temperature and pressure fields satisfy the inf-sup condition. This property guarantees the stability and convergence of the approximate solutions; compare [2, 31]. These finite elements can be defined as

$$V_h = \left\{ v_h \in C^0(\Omega) \quad v_h\big|_{\mathcal{K}_j} \in S(\mathcal{K}_j) \quad \forall\, \mathcal{K}_j \in \Omega_h \right\},$$
$$Q_h = \left\{ q_h \in C^0(\Omega) : \quad q_h\big|_{\mathcal{K}_j} \in R(\mathcal{K}_j) \quad \forall\, \mathcal{K}_j \in \Omega_h \right\},$$

where $C^0(\Omega)$ denotes the space of continuous and bounded functions in Ω, $S(\mathcal{K}_j)$ and $R(\mathcal{K}_j)$ are polynomial spaces defined in $\mathcal{K}_j$ as $S(\mathcal{K}_j) = P_2(\mathcal{K}_j)$ and $R(\mathcal{K}_j) = P_1(\mathcal{K}_j)$.

For the time integration of (2.6) we discretize the time interval into subintervals $[t_n, t_{n+1}]$, with length Δt and $t_n = n\Delta t$. We use the notation ω^n to denote the value of a generic function ω at time t_n. Hence, we formulate the finite element solutions to $\mathbf{u}^n(\mathbf{x})$, $T^n(\mathbf{x})$, and $p^n(\mathbf{x})$ as

$$(3.1) \qquad \mathbf{u}_h^n(\mathbf{x}) = \sum_{j=1}^{M} \mathbf{U}_j^n \phi_j(\mathbf{x}), \quad T_h^n(\mathbf{x}) = \sum_{j=1}^{M} \mathcal{T}_j^n \phi_j(\mathbf{x}), \quad p_h^n(\mathbf{x}) = \sum_{j=1}^{N} P_j^n \psi_j(\mathbf{x}),$$

where M and N are, respectively, the number of velocity/temperature and pressure mesh points in the partition Ω_h. The functions $\mathbf{U}_j^n$, $\mathcal{T}_j^n$, and P_j^n are the corresponding nodal values of $\mathbf{u}_h^n(\mathbf{x})$, $T_h^n(\mathbf{x})$, and $p_h^n(\mathbf{x})$, respectively. They are defined as $\mathbf{U}_j^n = \mathbf{u}_h^n(\mathbf{x}_j)$, $\mathcal{T}_j^n = T_h^n(\mathbf{x}_j)$, and $P_j^n = p_h^n(\mathbf{y}_j)$, where $\{\mathbf{x}_j\}_{j=1}^{M}$ and $\{\mathbf{y}_j\}_{j=1}^{N}$ are the set of velocity/temperature and pressure mesh points in the partition Ω_h, respectively, so that $N < M$ and $\{\mathbf{y}_1, \ldots, \mathbf{y}_N\} \subset \{\mathbf{x}_1, \ldots, \mathbf{x}_M\}$. In (3.1), $\{\phi_j\}_{j=1}^{M}$ and $\{\psi_j\}_{j=1}^{N}$ are the set of global nodal basis functions of V_h and Q_h, respectively, characterized by the property $\phi_i(\mathbf{x}_j) = \delta_{ij}$ and $\psi_i(\mathbf{y}_j) = \delta_{ij}$, with δ_{ij} denoting the Kronecker symbol.

The Galerkin-characteristic method we propose for approximating solutions to the LES equations (2.6) can be interpreted as a fractional step technique where the convective part is decoupled from the generalized Stokes/Boussinesq part in the time integration process. Thus, at each time step the new velocity, temperature, and

pressure are updated by first solving the convection equations

$$(3.2) \qquad \begin{aligned} \rho_\infty \frac{D\mathbf{u}}{Dt} &= \mathbf{0}, \\ \rho_\infty c_p \frac{DT}{Dt} &= 0, \end{aligned}$$

followed by the generalized Stokes/Boussinesq equations

$$(3.3) \qquad \begin{aligned} \nabla \cdot \mathbf{u} &= 0, \\ \rho_\infty \frac{\partial \mathbf{u}}{\partial t} + \nabla p &= \nabla \cdot \left(\left(2\mu + \mu_t\right) \mathbf{S}(\mathbf{u}) \right) + \mathbf{F}, \\ \rho_\infty c_p \frac{\partial T}{\partial t} &= \nabla \cdot \left(\left(\kappa + \kappa_t\right) \nabla T \right). \end{aligned}$$

The above procedure can be viewed as a stabilization technique for the conventional Galerkin finite element method where the LES equations (2.6) are integrated along the characteristic curves rather than in the time direction. In what follows, we formulate the numerical procedures for solving (3.2) and (3.3).

3.1. Formulation of convection fractional stage. To solve the convection equations (3.2) two steps are required, namely, the computation of characteristic trajectories and the interpolation procedure. Both steps are crucial to the overall accuracy of the Galerkin-characteristic method. For each mesh point $\mathbf{x}_j$, $j = 1, \ldots, M$, the characteristic curves $\mathbf{X}_{hj}^n := \mathbf{X}_h(\mathbf{x}_j, t_{n+1}; t_n)$ associated with (2.7) are the solutions of the initial-value problem

$$(3.4) \qquad \begin{aligned} \frac{d\mathbf{X}_h(\mathbf{x}_j, t_{n+1}; t)}{dt} &= \mathbf{u}_h \left(t, \mathbf{X}_h(\mathbf{x}_j, t_{n+1}; t)\right), \\ \mathbf{X}_h(\mathbf{x}_j, t_{n+1}; t_{n+1}) &= \mathbf{x}_j, \end{aligned}$$

where $\mathbf{u}_h(t, \mathbf{x})$ is the approximate flow velocity at time t. The solutions of (3.4) are known by departure points at time t of a fluid particle passing through the mesh point $\mathbf{x}_j$ at time $t = t_{n+1}$. To compute the departure points $\{\mathbf{X}_{hj}^n\}$, $j = 1, \ldots, M$, we write the solution of (3.4) as

$$(3.5) \qquad \mathbf{X}_{hj}^n = \mathbf{x}_j - \alpha_{hj},$$

where the displacement α_{hj} is calculated by the iterative procedure

$$(3.6) \qquad \begin{aligned} \alpha_{hj}^{(0)} &= \frac{\Delta t}{2} \left[3\mathbf{u}_h^n\left(\mathbf{x}_j\right) - \mathbf{u}_h^{n-1}\left(\mathbf{x}_j\right) \right], \\ \alpha_{hj}^{(k+1)} &= \frac{\Delta t}{2} \left[3\mathbf{u}_h^n\left(\mathbf{x}_j - \frac{1}{2}\alpha_{hj}^{(k)}\right) - \mathbf{u}_h^{n-1}\left(\mathbf{x}_j - \frac{1}{2}\alpha_{hj}^{(k)}\right) \right], \qquad k = 0, 1, \ldots, \end{aligned}$$

where the velocity values $\mathbf{u}_h^n\left(\mathbf{x}_j - \frac{1}{2}\alpha_{hj}^{(k)}\right)$ and $\mathbf{u}_h^{n-1}\left(\mathbf{x}_j - \frac{1}{2}\alpha_{hj}^{(k)}\right)$ are computed by the finite element interpolation (3.1) on the mesh element $\mathcal{K}_j$ where $\mathbf{x}_j - \frac{1}{2}\alpha_{hj}^{(k)}$ belongs. This procedure was first proposed in [30] for finite difference semi-Lagrangian methods and studied for finite elements in [7, 8], among others. It is also known that

$$(3.7) \qquad \left\| \alpha - \alpha^{(k+1)} \right\| \leq \frac{1}{4} \left\| \alpha - \alpha^{(k)} \right\| \|\nabla \mathbf{u}\| \Delta t, \quad k = 0, 1, \ldots,$$

where $\|\cdot\|$ denotes the Euclidean norm. Hence, a necessary condition for the convergence of iterations (3.6) is that the velocity gradient satisfies

$$(3.8) \qquad \|\nabla \mathbf{u}\| \, \Delta t < 1.$$

It should be stressed that, in our numerical results, the iterations in (3.6) were continued until the trajectory changed by less than 10^{-5}. However, in practice it is not recommended to repeat the iteration process more than a few times due to efficiency considerations.

Assuming that, for all $j = 1, \dots, M$, the pairs $(\mathbf{X}_{hj}^n, \hat{\mathcal{K}}_j)$, with $\hat{\mathcal{K}}_j$ is the mesh element where the characteristic foot $\mathbf{X}_{hj}^n$ is located, and the mesh point values $\{\mathbf{U}_j^n, \mathcal{T}_j^n\}$ are known, we compute the values $\{\hat{\mathbf{U}}_j^n, \hat{\mathcal{T}}_j^n\}$ as

$$(3.9) \qquad \hat{\mathbf{U}}_j^n := \mathbf{u}_h^n(\mathbf{X}_{hj}^n) = \sum_{k=1}^M \mathbf{U}_k \phi_k(\mathbf{X}_{hj}^n), \qquad \hat{\mathcal{T}}_j^n := T_h^n(\mathbf{X}_{hj}^n) = \sum_{k=1}^M \mathcal{T}_k \phi_k(\mathbf{X}_{hj}^n).$$

Then, the solution $\{\hat{\mathbf{u}}_h^n(\mathbf{x}), \hat{T}_h^n(\mathbf{x})\}$ of the convection stage (3.2) is obtained as

$$(3.10) \qquad \hat{\mathbf{u}}_h^n(\mathbf{x}) = \sum_{j=1}^M \hat{\mathbf{U}}_j^n \phi_j(\mathbf{x}), \qquad \hat{T}_h^n(\mathbf{x}) = \sum_{j=1}^M \hat{\mathcal{T}}_j^n \phi_j(\mathbf{x}).$$

Remark 1. It is worth remarking that the above convection fractional stage follows the flow by tracking the characteristics backward from a point $\mathbf{x}$ in a fixed mesh at the time step t_{n+1} to a point $\mathbf{X}$ at the previous time step t_n. Hence, the proposed procedure avoids the grid distortion problems present in forward-tracking methods. We should also mention that the Galerkin-characteristic method presented in [6, 21] suggests the evaluation of $\hat{\mathbf{u}}_h^n$ and $\hat{T}_h^n$ in (3.10) using an L^2-projection on the space of the velocity $V_h \times V_h$ and of temperature V_h, respectively. In many applications, the evaluation of integrals in the L^2-projection is difficult and computationally very demanding. An alternative approach was studied in [3] for convection-diffusion problems and was recently proposed in [24] for the shallow water equations.

Naturally, a Lagrangian interpolation of degree higher than one would not preserve monotonicity of the approximate solutions. In order to overcome this drawback, we incorporate to the Galerkin-characteristic solution (3.10) a limiting procedure. This implies that a solution value, obtained by interpolating in a grid element, lies between the maximum and minimum values in the vertices of this grid element. In this way we obtain a nonoscillatory algorithm at minor additional computational cost that possesses good shape preserving of the advected fields in the vicinity of strong gradients and maintains the order of convergence in regions where the solution is sufficiently smooth. Further details on this limiting procedure can be found in [7, 8].

Next, we formulate the resulting nonoscillatory algorithm for the solution of convective stage (3.2). For the simplicity of presentation, we formulate the algorithm only for the temperature variable, and similar work can be done for the velocity field. Thus, the numerical procedure to approximate the temperature solution $\hat{T}^n$ in (3.2) is carried out in the following steps:

1. Calculate the departure point $\mathbf{X}_{hj}^n$ using the procedure (3.5)-(3.6).
2. Identify the element $\hat{\mathcal{K}}_j$, where the characteristic foot $\mathbf{X}_{hj}^n$ is located.
3. Evaluate the high-order gridpoint approximation

$$(3.11) \qquad \hat{T}_{Hj}^n = \sum_{k=1}^{NH} \mathcal{T}_k \phi_k \left(\mathbf{X}_{hj}^n \right),$$

where $\{\phi_1, \ldots, \phi_{NH}\}$ are the quadratic local basis functions of the mesh element $\hat{\mathcal{K}}_j$.

4. Evaluate the low-order gridpoint approximation

$$(3.12) \qquad \hat{T}_{Lj}^n = \sum_{k=1}^{NL} \mathcal{T}_k \varphi_k \left(\mathbf{X}_{hj}^n \right),$$

where $\{\varphi_1, \ldots, \varphi_{NL}\}$ are the linear local basis functions of the element $\hat{\mathcal{K}}_j$. Observe that the linear interpolation preserves the monotonicity of the solution. Therefore, the numerical solution obtained by linear interpolation is free of oscillations and artificial extrema.

5. Update the solution $\hat{T}_j^n$ according to

$$(3.13) \qquad \hat{T}_j^n = \theta_j^n \hat{T}_{Hj}^n + (1 - \theta_j^n) \hat{T}_{Lj}^n,$$

where $\theta_j^n \in [0, 1]$, is a limiting coefficient chosen to control the amount of correction in the low-order approximation (3.12) in order to obtain a nonoscillatory solution. In the current study, it is defined as

$$(3.14) \qquad \theta_j^n = \begin{cases} \min \left(1, \dfrac{T_j^+ - \hat{T}_{Lj}^n}{\hat{T}_{Lj}^n - \hat{T}_{Hj}^n} \right), & \text{if} \quad \hat{T}_{Lj}^n - \hat{T}_{Hj}^n > 0, \\[2em] \min \left(1, \dfrac{T_j^- - \hat{T}_{Lj}^n}{\hat{T}_{Lj}^n - \hat{T}_{Hj}^n} \right), & \text{if} \quad \hat{T}_{Lj}^n - \hat{T}_{Hj}^n < 0, \\[2em] 1, & \text{if} \quad \hat{T}_{Lj}^n - \hat{T}_{Hj}^n = 0, \end{cases}$$

where T_j^+ and T_j^- are, respectively, the maximum and minimum solution values at the element $\hat{\mathcal{K}}_j$ which consist of the node j and its nearest neighbors at time t_n, i.e.,

$$T_j^+ = \max \left(T_{j1}^n, \ldots, T_{jNH}^n \right), \qquad T_j^- = \min \left(T_{j1}^n, \ldots, T_{jNH}^n \right).$$

Note that, by considering the limiting procedure (3.11)–(3.14), we force the interpolated value to remain within the largest and the smallest values of the solution in a set of points surrounding the feet of the characteristics, so that the interpolation procedure does not generate any extrema which is not possessed by the solution in a neighborhood of the departure points.

Remark 2. We should point out that the key idea used by the adjusted Galerkin-characteristic procedure (3.11)–(3.14) is inspired by the Zalesak flux-corrected transport technique reported in [32]. This technique consists of computing the mesh point values of the numerical solution by adding to the values of a low-order solution, which is monotone, a correction term that contains the contribution of a high-order solution and does not violate the monotonicity properties of the low-order solution. An example of low-order and high-order solution elements used in our computations is shown in Figure 3.1. In this case, the numbers of low-order and high-order local basis functions are $NL = 3$ and $NH = 6$, respectively.

3.2. Formulation of diffusion fractional step. To complete the implementation of the adjusted Galerkin-characteristic method for solving the LES equations (2.6), we consider a direct-type procedure to solve the Stokes/Boussinesq problem. The solution procedure consists of solving (3.3) for the velocity, pressure and temperature directly at each time step using a conjugate gradient method. Therefore, our method avoids projection techniques and does not require any special correction for the pressure. Note that, since the temperature is decoupled from the velocity using the convection fractional step, the conjugate gradient method is only adopted for the coupled pressure-velocity equations.

Hence, given a tolerance ε and using superscripts in parenthesis to indicate the iteration numbers, the Stokes/Boussinesq problem (3.3) is solved as follows:

1. Solve for $T_h^{n+1} \in V_h$ such that, for all $v_h \in V_h$,

$$\frac{\rho_\infty c_p}{\Delta t} \int T_h^{n+1} v_h \, d\Omega + \int (\kappa + \kappa_t) \nabla T_h^{n+1} \cdot \nabla v_h \, d\Omega =$$

$$(3.15) \qquad\qquad\qquad\qquad\qquad \frac{\rho_\infty c_p}{\Delta t} \int \hat{T}_h^n v_h \, d\Omega,$$

with $\mu_t = (c_s \Delta)^2 \|\mathbf{S}(\mathbf{u}_h^n)\|$ and $\kappa_t = \frac{\mu_t}{\sigma_T}$.

2. Given $p_h^{(0)} = p_h^n$, solve for $\mathbf{u}_h^{(0)} \in V_h \times V_h$ such that, for all $\mathbf{v}_h \in V_h \times V_h$,

$$\frac{\rho_\infty}{\Delta t} \int \mathbf{u}_h^{(0)} \mathbf{v}_h \, d\Omega + \int (2\mu + \mu_t) \mathbf{S}(\mathbf{u}_h^{(0)}) \cdot \nabla \mathbf{v}_h \, d\Omega = \frac{\rho_\infty}{\Delta t} \int \hat{\mathbf{u}}_h^n \mathbf{v}_h \, d\Omega +$$

$$(3.16) \qquad\qquad\qquad \int p_h^{(0)} \nabla \cdot \mathbf{v}_h \, d\Omega + \int \mathbf{F}_h^{n+1} \mathbf{v}_h \, d\Omega.$$

Then, compute

$$r_h^{(0)} = \nabla \cdot \mathbf{u}_h^{(0)}.$$

3. Solve for $\psi_h^{(0)} \in Q_h$ such that, for all $\phi_h \in Q_h$,

$$\int_\Omega \nabla \psi_h^{(0)} \cdot \nabla \phi_h d\Omega = \int_\Omega r_h^{(0)} \phi_h d\Omega,$$

and set

$$g_h^{(0)} = \frac{\rho_\infty}{\Delta t} \psi_h^{(0)} + (2\mu + \mu_t) r_h^{(0)}, \qquad\qquad \omega_h^{(0)} = g_h^{(0)}.$$

For $m \geq 0$, assume that $p_h^{(m)}, \mathbf{u}_h^{(m)}, r_h^{(m)}, g_h^{(m)}, w_h^{(m)}$ are known, we compute $p_h^{(m+1)}, \mathbf{u}_h^{(m+1)}, r_h^{(m+1)}, g_h^{(m+1)}, w_h^{(m+1)}$ as follows:

(a) Solve for $\bar{\mathbf{u}}_h \in V_h \times V_h$ such that, for all $\mathbf{v}_h \in V_h \times V_h$,

$$\frac{\rho_\infty}{\Delta t} \int \bar{\mathbf{u}}_h^{(m)} \mathbf{v}_h \, d\Omega + \int (2\mu + \mu_t) \mathbf{S}(\bar{\mathbf{u}}_h^{(m)}) \cdot \nabla \mathbf{v}_h \, d\Omega =$$

$$(3.17) \qquad\qquad\qquad\qquad\qquad \int \omega_h^{(m)} \nabla \cdot \mathbf{v}_h \, d\Omega,$$

with $\mu_t = (c_s \Delta)^2 \left\|\mathbf{S}(\mathbf{u}_h^{(m)})\right\|$. Then, set

$$\bar{r}_h^{(m)} = \nabla \cdot \bar{\mathbf{u}}_h^{(m)}.$$

(b) Compute

$$\rho_m = \frac{\displaystyle\int r_h^{(m)} g_h^{(m)} \, d\Omega}{\displaystyle\int \bar{r}_h^{(m)} \omega_h^{(m)} \, d\Omega}.$$

(c) Set

$$p_h^{(m+1)} = p_h^{(m)} - \rho_m \omega_h^{(m)}, \qquad \mathbf{u}_h^{(m+1)} = \mathbf{u}_h^{(m)} - \rho_m \bar{\mathbf{u}}_h^{(m)},$$

$$r_h^{(m+1)} = r_h^{(m)} - \rho_m \bar{r}_h^{(m)}.$$

(d) Solve for $\bar{\psi}_h^{(k)} \in S_h$ such that, for all $\phi_h \in S_h$,

$$\int \nabla \bar{\psi}_h^{(m)} \cdot \nabla \phi_h \, d\Omega = \int \bar{r}_h^{(m)} \phi_h \, d\Omega,$$

and set

$$g_h^{(m+1)} = g_h^{(m)} - \rho_m \left(\frac{\rho_\infty}{\Delta t} \psi_h^{(m)} + (2\mu + \mu_t) \, r_h^{(m)} \right).$$

  i. If $\quad \dfrac{\displaystyle\int r_h^{(m+1)} g_h^{(m+1)} \, d\Omega}{\displaystyle\int r_h^{(0)} g_h^{(0)} \, d\Omega} \leq \varepsilon$, then

$$p_h^{n+1} = p_h^{(m+1)}, \qquad \mathbf{u}_h^{n+1} = \mathbf{u}_h^{(m+1)},$$

  stop.
  ii. Else, compute

$$\eta_m = \frac{\displaystyle\int r_h^{(m+1)} g_h^{(m+1)} \, d\Omega}{\displaystyle\int r_h^{(m)} g_h^{(m)} \, d\Omega}, \qquad \omega_h^{(m+1)} = g_h^{(m+1)} + \eta_m \omega_h^{(m)},$$

  change $m \longleftarrow m+1$, return to step (a) and repeat.
  iii. End if.

Note that (3.17) and (3.15) have to be solved subject to appropriate boundary conditions associated with the LES equations (2.6). Furthermore, the above time stepping is only first-order accurate, and a second-order accuracy in time can be achieved by using the Crank–Nicolson method. A detailed formulation of this method for laminar incompressible Navier–Stokes has been described in [7, 10], whereas its analysis of convergence and stability has been carried out in [9].

Remark 3. It is noteworthy that the above iterative process requires a solution of uncoupled elliptic problems such that their finite element discretization leads to well-conditioned linear systems of algebraic equations for which very efficient solvers can be implemented. Therefore, by taking advantage of these properties, we can solve the linear systems in the Galerkin-characteristic algorithm by conjugate gradient solvers

using an incomplete Cholesky factorization. This yields a very powerful and efficient method for solving this class of linear systems of algebraic equations.

The finite element discretization of (3.17)–(3.15) is trivial and is omitted here. It is described in many text books; compare [15], among others. In addition, the detailed integration of similar equations for triangular elements was presented in [3] for convection-diffusion problems and in [24] for shallow water equations.

4. Numerical examples. We present numerical results for two examples in turbulent convection flows and heat transport. The main goals of this section are to illustrate the numerical performance of the Galerkin-characteristic algorithm described above and to numerically verify its capability to solve turbulent convection flow problems. In all of the computations reported herein, the linear systems of algebraic equations are solved using the conjugate gradient solver with incomplete Cholesky decomposition. In addition, all stopping criteria for iterative solvers were set to 10^{-5}, which is small enough to guarantee that the algorithm truncation error dominated the total numerical error. In our Galerkin-characteristic algorithm, the number of iterations to reach this tolerance do not overpass 20 iterations in the examples considered. All of the computations are performed on a Pentium personal computer with one processor of 2.2 GB of RAM and 1.8 GHz.

4.1. Accuracy example. As a first example, we consider the advection-diffusion problem of rotating a Gaussian pulse in an uniform rotating flow field. This problem was presented in [28] and has been widely used to quantify the errors in characteristics-based methods. The problem statement is given by

$$(4.1) \qquad \frac{\partial u}{\partial t} + \mathbf{v} \cdot \nabla u - \nu \Delta u = 0,$$

equipped with the following initial data

$$(4.2) \qquad u(x, y, 0) = 100 \exp\Big(-\frac{(x - x_0)^2 + (y - y_0)^2}{2\sigma^2}\Big).$$

The computational domain is a 3200 $km \times$ 3200 km squared domain, the velocity field $\mathbf{v} = (v_1, v_2)^T$, where $v_1 = -\omega y$ and $v_2 = \omega x$, with $\omega = 10^{-5}/s$ being the angular velocity. Here, initial and boundary conditions are derived from the analytical solution

$$u(x, y, t) = \frac{100}{1 + \frac{2\nu t}{\sigma^2}} \exp\Big(-\frac{\bar{x}^2 + \bar{y}^2}{2(\sigma^2 + 2\nu t)}\Big),$$

where $\bar{x} = x - x_0 \cos \omega t + y_0 \sin \omega t$, $\bar{y} = y - x_0 \sin \omega t - y_0 \cos \omega t$, $(x_0, y_0) = (-800\ km, 0)$ is the center of the initial Gaussian hill and $\sigma^2 = 2 \times 10^4\ km^2$. The diffusion coefficient ν is allowed to take the values $10^4\ m^2/s$ and $0\ m^2/s$, whereas the time step Δt is set to $\overline{\Delta t} = 4 \times 10^4\ s$. We denote by GC the conventional Galerkin-characteristic method obtained by setting $\theta_j^n = 1$ in (3.13), while by GCA we refer to the Galerkin-characteristic method with adjustment (3.13)–(3.14).

In Table 4.1 we list the CPU time (in seconds), relative root mean square error (RMS), minimum (Min), maximum (Max), and mass (Mass) of the numerical solution. We present results after 10 revolutions of the Gaussian hill and for two time steps using meshes with a different number of gridpoints. Note that the time period required for one complete rotation is $\frac{2\pi}{\omega}$. As can be seen from this table, for the mesh with 32×32 gridpoints, the GC method goes unstable (—— in Table 4.1 corresponds to runs where the GC method becomes unstable). In terms of RMS error the results obtained using

TABLE 4.1

Results for advection-diffusion of the rotating Gaussian pulse after 10 *revolutions using different meshes and two time steps with* $\overline{\Delta t} = 4 \times 10^4$ *s. Remark that the analytical maximum is* 99.37 *and* 100 *for* $\nu = 10^4 \ m^2/s$ *and* $\nu = 0 \ m^2/s$, *respectively. Here, the CPU time is given in seconds.*

| | | $\Delta t = \overline{\Delta t}$ | | | | | | | | | |
| | | GC method | | | | | GCA method | | | | |
ν	Mesh	Min	Max	RMS	Mass	CPU	Min	Max	RMS	Mass	CPU
10^4	32×32	——	——	——	——	——	0	37.72	0.5316	98.94	0.71
	64×64	−0.57	79.52	0.1390	85.95	2.42	0	73.97	0.1604	99.17	2.53
	128×128	−0.03	97.89	0.0123	90.99	9.46	0	96.93	0.0123	99.29	9.58
	256×256	−0.0001	99.27	0.0008	95.77	40	0	98.83	0.0011	99.33	41
0	32×32	——	——	——	——	——	0	37.79	0.5333	99.01	0.69
	64×64	−0.58	79.87	0.1405	87.03	2.47	0	74.26	0.1618	99.77	2.46
	128×128	−0.06	98.52	0.0125	92.14	9.47	0	97.43	0.0126	99.95	9.84
	256×256	−0.004	99.89	0.0009	98.86	40	0	99.38	0.0011	99.99	42

| | | $\Delta t = \frac{\overline{\Delta t}}{2}$ | | | | | | | | | |
| | | GC method | | | | | GCA method | | | | |
ν	Mesh	Min	Max	RMS	Mass	CPU	Min	Max	RMS	Mass	CPU
10^4	32×32	——	——	——	——	——	0	21.89	0.7390	98.23	1.26
	64×64	−2.39	106.99	0.7908	80.09	4.58	0	63.47	0.2888	98.99	4.64
	128×128	−0.86	96.46	0.0235	88.63	18	0	94.98	0.0251	99.19	18.35
	256×256	−0.002	99.13	0.0029	93.71	77	0	98.55	0.0032	99.28	79
0	32×32	——	——	——	——	——	0	21.91	0.7402	98.99	1.27
	64×64	−2.56	130.59	0.9430	83.88	4.57	0	63.66	0.2906	99.75	4.75
	128×128	−2.46	97.04	0.0250	91.59	18	0	95.52	0.0254	99.86	18.4
	256×256	−0.12	99.75	0.0030	96.23	78	0	99.13	0.0033	99.93	79

the GC and GCA methods are roughly similar. From the values of Min and Max in Table 4.1, we observe higher and negative values for the GC method which are avoided in GCA results. Concerning the mass conservation, Table 4.1 shows that, for pure advection at mesh of 128×128 gridpoints, the GC method lost more than 7% of the initial mass after the 10 rotations, whereas the GCA method is mass conserving at the machine precision. This clearly demonstrates that the limiting procedure does not deteriorate the accuracy of the GC method. An examination of the CPU time in Table 4.1 reveals that, on coarse meshes, there is no noticeable difference between the computational cost required for both methods. In all results given in Table 4.1, the CPU time needed for the GCA method is less than 1.1 times more than that needed for the GC method. It is evident that the additional computational effort used by the limiting procedure has been kept to the minimum that the GCA algorithm is still effective.

Taking all factors into account, we conclude that, for the considered test example, the GCA method demonstrates higher monotone and nonoscillatory properties than the GC method. More importantly, a balance between efficiency and accuracy in both algorithms benefits the GCA method, since the additional cost required for the limiting procedure in GCA algorithm is minimal while the results obtained by the GCA method are more accurate than those obtained by the GC method. Therefore,

TABLE 4.2
Comparison of average Nusselt numbers on the cavity walls at different Reynolds numbers.

	$Re = 5 \times 10^4$		$Re = 2 \times 10^5$		$Re = 4 \times 10^5$	
	GCA method	Ref. [20]	GCA method	Ref. [20]	GCA method	Ref. [20]
$\overline{Nu}_l$	67.827	68.560	108.227	109.696	128.1350	128.550
$\overline{Nu}_r$	41.774	39.422	82.508	80.558	105.502	99.412
$\overline{Nu}_b$	18.472	18.854	58.401	59.133	78.253	78.844
$\overline{Nu}_t$	17.096	15.426	57.395	56.562	76.051	75.416

hereafter we shall focus our attention on numerical simulations carried out using only the GCA method.

4.2. Mixed convection in a cavity. Our second example is the problem of turbulent mixed convection in a lid-driven squared cavity with length $L = 1$. This test problem has been numerically studied in [20], and experimental data have also been provided in [19]. The left and right vertical walls are maintained at dimensionless hot temperature $T = 1$ and cold temperature $T = 0$, respectively. The bottom and top horizontal walls are insulated. According to [20], the left wall is moving with a velocity $v = 1$, for which the Reynolds number $Re = 1/\nu$. The problem is tested with the Prandtl number $Pr := \nu/\kappa = 0.71$, the Smagorinsky constant $c_s = 0.1$, and for Reynolds numbers $Re = 5 \times 10^4$, 10^5, and 2×10^5. The spatial domain is discretized into 128×128 gridpoints, and numerical results are presented at steady-state time using a time step $\Delta t = 0.1$.

The purpose of this example is to present a quantitative study of the GCA method by a comparison of the computed results to those provided from experimental data. To this end, we summarize in Table 4.2 a comparison between published results for average Nusselt numbers on the cavity walls and results obtained with the GCA method. Recall that the average Nusselt numbers $\overline{Nu}_l$ and $\overline{Nu}_r$ on the left and right walls of the cavity are calculated as

$$\overline{Nu}_l = -\int_0^L \kappa \frac{\partial T}{\partial x}\bigg|_{x=0} dy \qquad \text{and} \qquad \overline{Nu}_r = -\int_0^L \kappa \frac{\partial T}{\partial x}\bigg|_{x=L} dy,$$

respectively. A similar formula has been used to calculate the average Nusselt numbers $\overline{Nu}_b$ and $\overline{Nu}_t$ on the bottom and top walls. The obtained results mostly compared favorably with all of the model results from references [20, 19]. As it is obvious from the Table 4.2, the small differences in comparison with other methods can be attributed to the nature of the turbulence model used in computations. It should be noted that the authors in [20] used the Reynolds-averaged Navier–Stokes model to compute the effective viscosity and the thermal conductivity.

Figure 4.1 shows the streamlines, velocity vectors, and isotherms obtained for different Reynolds numbers. As can be seen, the flow exhibits recirculating regions in the cavity corners and the structure of these recirculating regions is strongly influenced by the values of Reynolds numbers. In addition, the vertex center is very close to the geometrical center of the cavity for all of the Reynolds numbers. The convective heat transfer in recirculating flow is also affected by Reynolds numbers. There is excellent agreement between the presented numerical results and the numerical predictions [20] and the experimental results [19] available in the literature. Note that the performance of our numerical model is very attractive, since the computed solutions remain stable
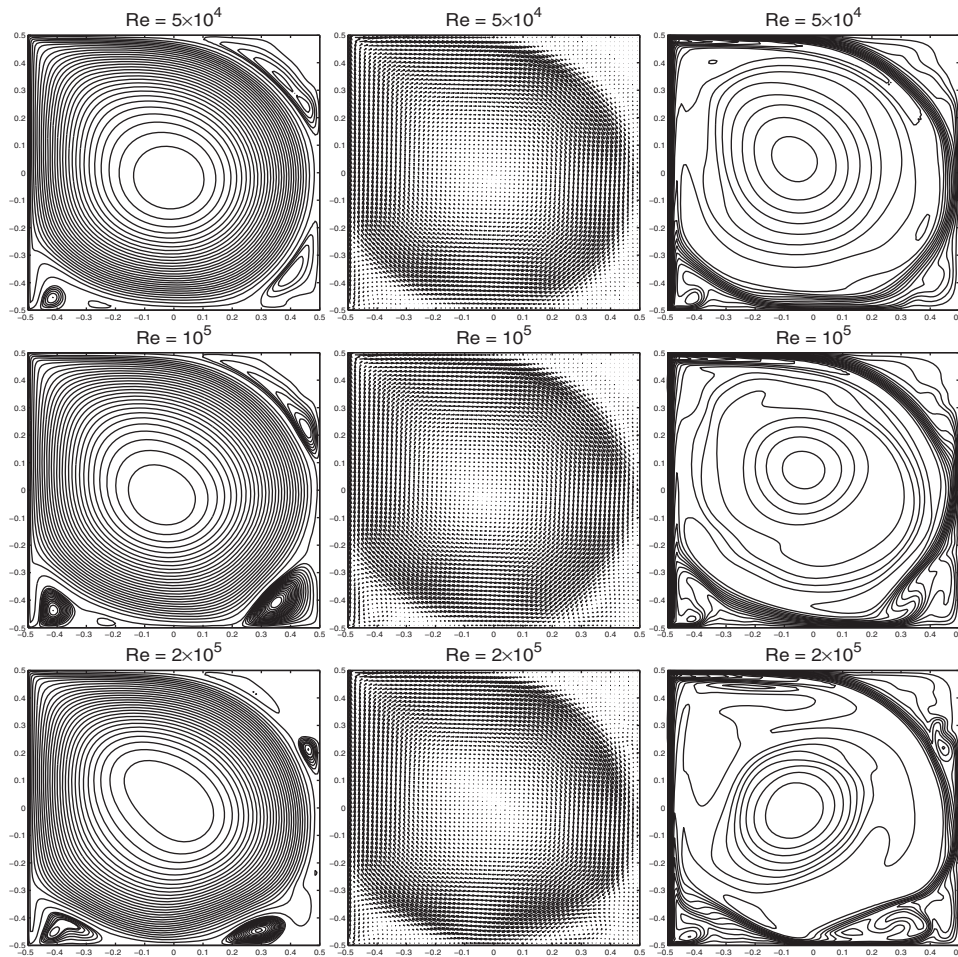
FIG. 4.1. *Streamlines (left column), velocity field (middle column), and isotherms (right column) for lid-driven cavity flow. From top to bottom:* $Re = 5 \times 10^4$, $Re = 10^5$, *and* $Re = 2 \times 10^5$.

and highly accurate even for relatively coarse grids without solving nonlinear systems or requiring special stabilization techniques.

The profiles of the u-velocity component along the vertical center line and the v-velocity component along the horizontal center line are shown in Figure 4.2 for $Re = 2 \times 10^5$. In this figure, we have also included numerical predictions from [20] and experimental data from [19]. The boundary layers for the velocity components can be clearly observed. There is excellent agreement between the computed results and those published in [20, 19]. Furthermore, computed vortex strengths and temperature distribution on the cavity walls are found to be consistent with those obtained for lid-driven squared cavity flow at corresponding Reynolds numbers. These features clearly demonstrate the high accuracy achieved by the proposed GCA method for solving turbulent mixed convection flows in the lid-driven squared cavity.

4.3. Mixed convection flow in the Strait of Gibraltar. Our final test example is the mixed convection flow and heat transport in the Strait of Gibraltar. The mean flow in the Strait of Gibraltar has been the subject of numerous numerical inves-
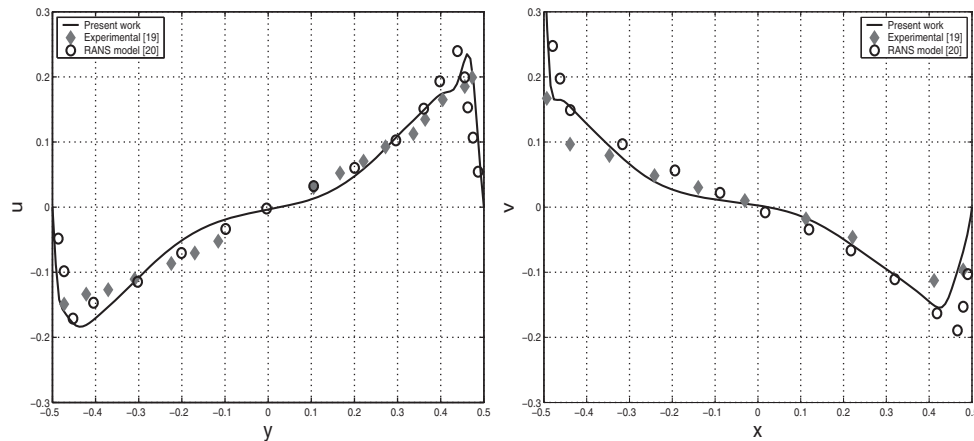
FIG. 4.2. *The velocity component u at vertical center line (left plot), and the velocity component v at horizontal center line (right plot) for* $\mathrm{Re} = 2 \times 10^5$.
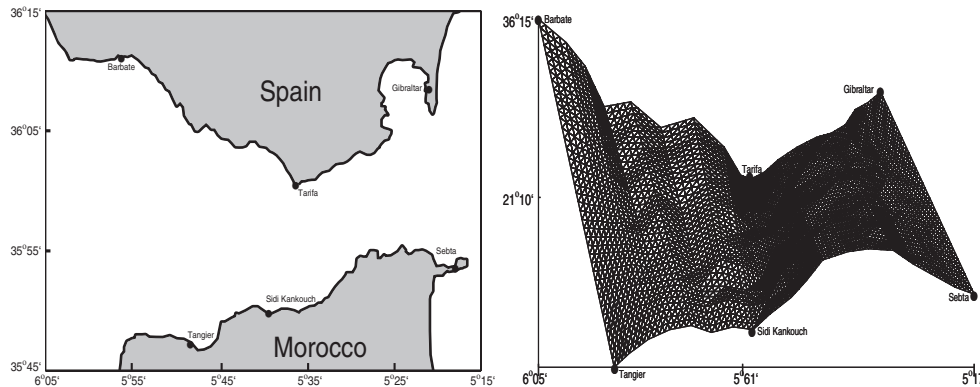
FIG. 4.3. *Schematic description of the Strait of Gibraltar along with some well-known locations in the Strait (left), and the domain configuration used in the numerical simulations (right).*

tigations; we refer to [1] for a survey and more details. Most of the studies carried out on the Strait of Gibraltar used the shallow water equations to model the mean flow, and no thermal effects have been taken into account. However, observations reported in [18] indicate that water level in the sea surface is driven by temperature changes, while the deeper layer's salinity also become important. Furthermore, authors in [22] claimed that the sea-surface temperature is considered to play an important role in the Mediterranean circulation through the Strait of Gibraltar. The sea-surface temperatures are maxima in summer (August–September) with average values of 23–24$^\circ C$ and minima in winter (January–February) with averages of 11–12$^\circ C$. The North Atlantic water is about 5–6$^\circ C$ colder than the Mediterranean water; elaborate details are available in [22, 18], among others. The purpose of this example is twofold, on one hand to test the capability of the GCA method to handle complex geometry and moving fronts, and, on the other hand, to develop mathematical tools to study convective heat transport in the Strait of Gibraltar.

The Strait of Gibraltar (see Figure 4.3) is bounded to the north and south by the Iberian and African continental forelands, and to the west and east by the Atlantic

TABLE 4.3
Dimensional quantities used in mixed convection flow and heat transport in the Strait of Gibraltar.

Quantity	Symbol	Unit	Typical reference value
Reference density	ρ_∞	kg/m^3	$1000\ kg/ms^3$
Viscosity	μ	kg/ms	$1.14 \cdot 10^{-3}\ kg/ms$
Specific heat	c_p	kJ/kgK	$4180\ kJ/kgK$
Coefficient of thermal expansion	β	$/C$	$210 \cdot 10^{-6}\ /C$
Thermal diffusivity	κ	m^2/s	$0.14 \cdot 10^{-6}\ m^2/s$
Gravity acceleration	g	m/s^2	$9.81\ m/s^2$
Average cold temperature	T_C	$^\circ C$	$17\ ^\circ C$
Average hot temperature	T_H	$^\circ C$	$23\ ^\circ C$
Reference temperature	T_∞	$^\circ C$	$20\ ^\circ C$
Reference height	x_∞	km	$14\ km$
Reference velocity	u_∞	m/s	$0.54\ m/s$
Simulation time interval	$\mathbb{T}$	h	$24\ h$

Ocean and the Mediterranean Sea, respectively. The Mediterranean circulation is forced by water exchange through the Strait of Gibraltar, by wind stresses, and by buoyancy flux at the surface due to fresh-water and heat fluxes. In general, the basic circulation in the Strait of Gibraltar consists on an upper layer of cold, fresh surface Atlantic water and an opposite deep current of warmer, salty Mediterranean outflowing water; see, for example, [1]. The system is about 60 Km long between its west Barbate–Tangier section and its east Gibraltar–Sebta section. Its width varies from a minimum of about 14 Km at Tarifa–Punta Cires section and a maximum of 44 Km at Barbate–Tangier section. The topography of the Strait is very complex with a maximum depth less than 1 Km; compare [1, 14, 13]. Here we assume that the flow is two-dimensional, and the Bousinesq approximation is valid. Indeed, the validity of these assumptions is supported by the fact that the depth of the Strait of Gibraltar is smaller than its width, and the temperature difference between the Mediterranean water and the Atlantic water is small. In addition, Mediterranean outflow is much less buoyant than Atlantic water at the same depth, and therefore it cascades down to around one Km depth in the Atlantic Ocean.

Hence, the problem statement consists of solving (2.6) in the computational domain shown in the right plot of Figure 4.3. The model is started from warm rest, i.e., $T = T_C$ and $\mathbf{u} = \mathbf{0}$. Here, the temperature fields of the Atlantic and Mediterranean waters have been obtained from an average of the spring data [22]. At the left and right boundary regions we use cold temperature T_C and hot temperature T_H, respectively. The top and bottom coastlines are considered as adiabatic boundaries. For the water flow, a well-developed velocity profile, with a maximum velocity u_∞ is imposed at the western entrance of the Strait of Gibraltar. This profile corresponds to the annual mean of the Atlantic input flux [1], and it is also comparable to the flow generated by the main semidiurnal M_2 tide; see, for example, [14, 13]. At the eastern exit of the Strait of Gibraltar, we impose the pseudostress condition

$$-p\mathbf{n} + \mu\frac{\partial \mathbf{u}}{\partial \mathbf{n}} = \mathbf{0},$$

where $\mathbf{n}$ denotes the unit outward normal vector on the boundary. On the remaining boundaries we impose no-slip boundary conditions. The dimensional quantities in (2.6) and the reference values are summarized in Table 4.3. Note that, unlike the
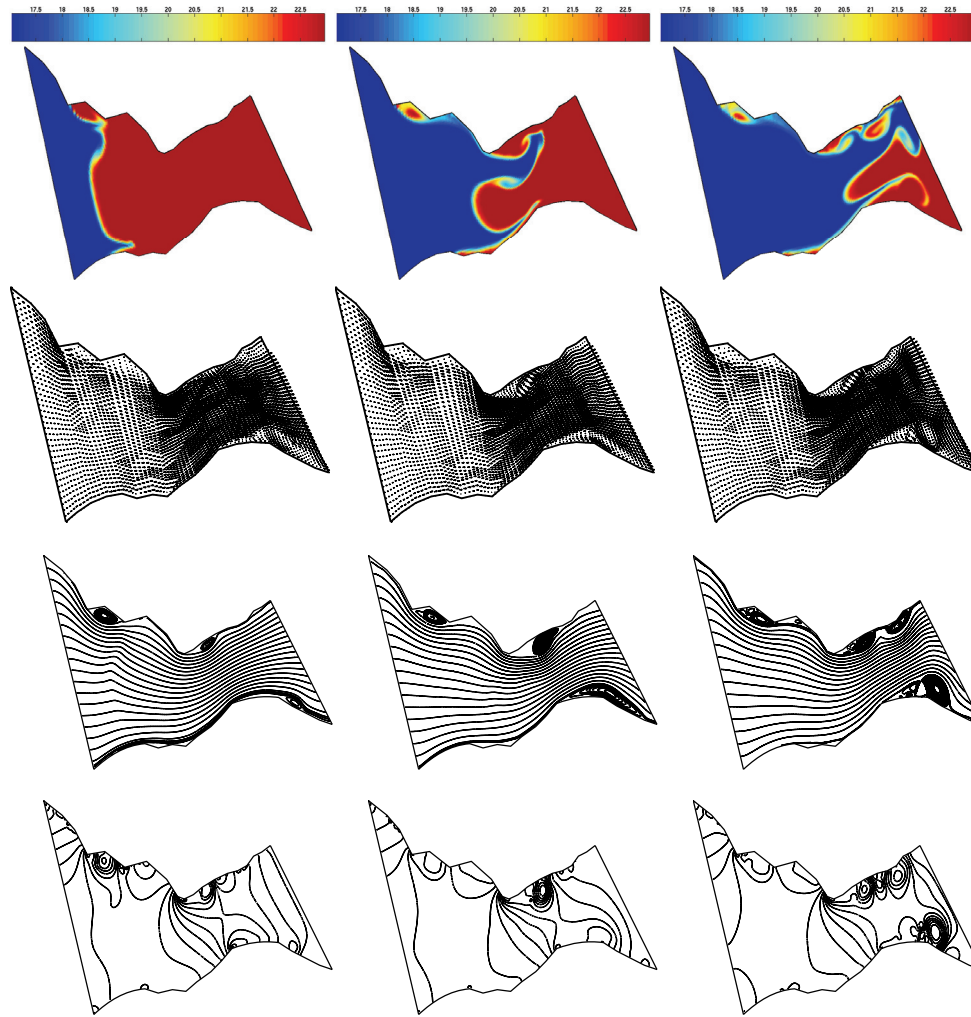
FIG. 4.4. *Results for mixed convection flow and heat transport in the Strait of Gibraltar at time* $t = \mathbb{T}/4$ *(left),* $t = \mathbb{T}/2$ *(middle), and* $t = \mathbb{T}$ *(right). From top to bottom: temperature snapshots (first row), velocity vectors (second row), streamlines (third row), and pressure contours (fourth row).*

previous test example, the considered mixed convection is a problem unsteady in nature with moving regions of strong gradients, and therefore good numerical accuracy is required in order to capture the different phenomena present in its evolving solution. As a consequence, the later turbulent flow is more difficult to handle; the results shown here illustrate the robustness of the GCA method.

In Figure 4.4 we display the temperature distribution, velocity vectors, streamlines field, and pressure contours at three different times, namely, $t = \mathbb{T}/4$, $t = \mathbb{T}/2$, and $t = \mathbb{T}$ using a fixed time step $\Delta t = 100\ s$ and the Smagorinsky constant $c_s = 0.18$. At an earlier time of the simulation, the cold Atlantic front entering the Strait of Gibraltar starts to develop and is advected later on by the flow at the far exit of the Strait of Gibraltar. The interaction between the heat transfer and the water flow is detected across the Strait of Gibraltar during the simulation time. It can be clearly seen that the complicated temperature and flow structures being captured by the

GCA method. Particularly, we can see that two major vortices are located near the Tarifa narrow and Sebta basin. Inside these vortices, there is a more complex vortex pattern. The decrease and increase of the strengths of vortices with time can be seen in Figure 4.4.

From the computed results we can observe that, for the considered flow and heat conditions, the temperature is transported towards the Spanish coast. The cold front follows the stream induced by the mean flow entering the Strait of Gibraltar from the Atlantic Ocean. During its advection, the thermal plume alerts the flow structure developing recirculation zones with a different order of magnitude in the vicinity of Tarifa narrow. The downstream recirculation zone near Sebta basin is mainly due to the temperature differences at the region near the exit boundary. In summary, the heat transport is captured accurately, the flow field is resolved reasonably well, and the temperature front is shape preserving. All of these features have been achieved using time steps larger than those required for Eulerian-based methods in convection-dominated flows. The presented results demonstrate that the GCA method is suited for the prediction of an LES of sea-surface temperature dispersion in the Strait of Gibraltar. It should be stressed that results from the proposed LES model should be compared with observations of real sea-surface temperatures in the Strait of Gibraltar. However, there is no data available until now to carry out this work. Thus, at the moment we can only perform simulations and verify that results are plausible and consistent.

We now turn our attention to the sensibility of the LES on the Smagorinsky constant c_s. To this end, we perform a series of simulations using different values of c_s, and we report in Figure 4.5 the time evolution of the corresponding kinetic energy at the Tarifa narrow. This figure gives an idea of the evolution of the kinetic energy as the thermal plume moves with time subject to different Smagorinsky constants in the LES model. It is clear that larger values of Smagorinsky constant results in longer fluctuations in the kinetic energy before this later stabilizes to a stationary state. It is evident that further investigations on the influence of the Smagorinsky constant and the filter width on the LES results are needed.

As a final remark we want to comment on the numerical results (not reported here) obtained using the conventional Galerkin algorithm (GA) method. Using this method, the temperature variable exhibits larger values than T_H and smaller values than T_C. The relevance of the property that $T \in [T_C, T_H]$ for this problem is twofold. Firstly, since no thermal source is present in the LES system, to obtain larger values than T_H and smaller values than T_C is physically unacceptable. Secondly, when the thermal diffusivity is as small as the one of the current problem, having larger values than T_H and smaller values than T_C may cause a breakdown in the iterations of the conjugate gradient solver used to solve the linear systems for the Stokes/Boussinesq stage in the conventional GC algorithm. In the opposite, results obtained using the proposed GCA method are free from any spurious oscillations, and the computed temperature is found to be monotone and bounded in $[T_C, T_H]$ during the time integration process. In fact, the GCA solution reveals the physics well in this test example.

Finally, we give an average distribution of the CPU time spent for each stage of the GCA algorithm for this problem: convection fractional stage 17% and diffusion fractional step 79%; within the convection fractional stage, only 4% of the CPU time is consumed by the limiting process in the GCA method. It should be pointed out that most of the computational effort goes into solving the linear systems in the generalized Stokes/Boussinesq stage of the GCA algorithm. Therefore, reducing the CPU time in the GCA method can be achieved by constructing a more efficient preconditioned
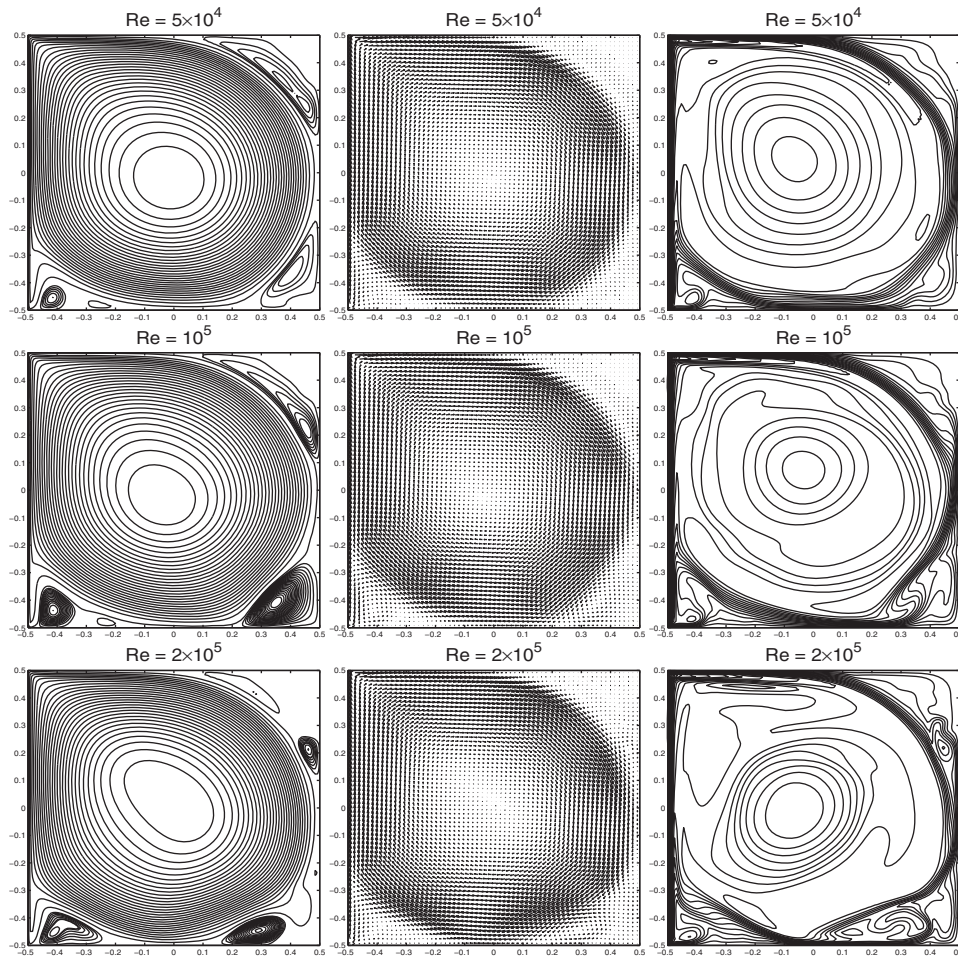
FIG. 4.5. *Time evolution of the kinetic energy at the Tarifa narrow using different values of c_s.*

iterative solver for these linear systems. Multigrid techniques are known to be the most efficient methods for solving linear systems and can therefore be the suitable tools to increase the efficiency of the GCA method. Needless to say, that the CPU time in the proposed GCA method can be drastically reduced if parallel computers were used.

5. Summary and conclusions. A Galerkin-characteristic method has been developed for LES of turbulent flow and heat transfer. The equations are based on thermal incompressible Navier–Stokes equations subject to the Boussinesq approximation. For turbulence effects we have considered the Smagorinsky subgrid model. The method combines the modified method of characteristics with a Galerkin finite element discretization in primitive variables. A conjugate gradient algorithm has been implemented for the solution of the generalized Stokes/Boussinesq problem. This method avoids projection techniques and does not require any special correction for the pressure. We have also showed how a limiting process can be implemented for the Galerkin-characteristic algorithm in order to preserve monotonicity of the computed solution. Numerical results presented in this work have shown the ability of

the current Galerkin-characteristic algorithm to perform very well in the presence of strong gradients and discontinuities without nonphysical oscillations and numerical diffusion; even coarse meshes and large timesteps are used in computations.

Numerical experiments were conducted to solve the advection-diffusion example of a Gaussian hill and the example of mixed convection flow in a lid-driven cavity. The proposed method has also been verified for the numerical simulation of turbulent flow and heat transport in the Strait of Gibraltar. In the first example, the accuracy and efficiency of conventional and adjusted Galerkin-characteristic methods have been compared, whereas the computed results from the adjusted Galerkin-characteristic method have been compared to measurements in the second test problem. The last example represents a practical demonstration of the capabilities of the Galerkin-characteristic method in simulations of coupled turbulent flow and heat transfer for two major reasons. Firstly, the computational domain in the Strait of Gibraltar is a large-scale domain including well-defined shelf regions. Secondly, the Strait of Gibraltar contains complex fully two-dimensional eddy viscosity and moderate temperature difference, which present a challenge for most numerical methods used in thermal flow modelling. For all of these examples, the algorithm exhibited good shape and high accuracy; excellent agreement has been found between the computed results and those published on mixed convection in a squared cavity, with stability behavior even large timesteps are used in computations. The presented results demonstrate the capability of the Galerkin-characteristic method that can provide insight to complex turbulent thermal flow behaviors.

Finally, it should be stressed that the stability limitations of the Galerkin-characteristic method are usually due to errors in the approximation of the trajectories, specifically in the location of the departure points at the feet of the characteristic curves. Future work will concentrate on the extension of this method to coupled turbulent flow and heat transfer problems in three space dimensions.

REFERENCES

[1] J.I. ALMAZÁN, H. BRYDEN, T. KINDER, AND G. PARRILLA, EDS., *Seminario Sobre la Oceanografía Física del Estrecho de Gibraltar*, SECEG, Madrid, 1988.

[2] M, BERCOVIER AND O. PIRONNEAU, *Error estimates for finite element solution of the Stokes problem in the primitive variables*, Numer. Math., 33 (1979), pp. 211–224.

[3] R. BERMEJO AND M. EL-AMRANI, *A finite element semi-Lagrangian explicit Runge-Kutta-Chebyshev method for convection dominated reaction-diffusion problems*, J. Comput. Appl. Math., 154 (2003), pp. 27–61.

[4] L.C. BERSELLI, T. ILIESCU, AND W.J. LAYTON, *Mathematics of Large Eddy Simulation of Turbulent Flows*, Springer, New York, 2006.

[5] A. CHATELAIN, F. DUCROS, AND O. METAIS, *LES of turbulent heat transfer: Proper convection numerical schemes for temperature transport*, Internat. J. Numer. Methods Fluids, 44 (2004), pp. 1017–1044.

[6] J. DOUGLAS AND T.F. RUSSELL *Numerical methods for convection-dominated diffusion problems based on combining the method of characteristics with finite elements or finite difference procedures*, SIAM J. Numer. Anal., 19 (1982), pp. 871–885.

[7] M. EL-AMRANI AND M. SEAÏD, *A finite element modified method of characteristics for convective heat transport*, Numer. Methods Partial Differential Equations, 24 (2008), pp. 776–798.

[8] M. EL-AMRANI AND M. SEAÏD, *Eulerian–Lagrangian time-stepping methods for convection-dominated problems*, Internat. J. Comput. Math., 85 (2008), pp. 421–439.

[9] M. EL-AMRANI AND M. SEAÏD, *Convergence and stability of finite element modified method of characteristics for the incompressible Navier-Stokes equations*, J. Numer. Math., 15 (2007), pp. 101–135.

[10] M. EL-AMRANI AND M. SEAÏD, *Numerical simulation of natural and mixed convection flows by Galerkin-characteristic method*, Internat. J. Numer. Methods Fluids., 53 (2007), pp. 1819–1845.

[11] M. El-Amrani and M. Seaïd, *Weakly compressible and advection approximations of incompressible viscous flows*, Comm. Numer. Methods Engrg., 22 (2006), pp. 831–847.

[12] B.J. Geurts, *Elements of Direct and Large-eddy Simulation*, Edwards, Philadelphia, 2004.

[13] M. González and M. Seaïd, *Finite element modified method of characteristics for shallow water flows: Application to the Strait of Gibraltar*, Prog. Ind. Math., 8 (2005), pp. 518–522.

[14] M. González and A. Sánchez-Arcilla, *Un modelo numérico en elementos finitos para la corriente inducida por la marea. Aplicaciones al Estrecho de Gibraltar*, Revista Internacional de Métodos Numéricos para Cálculo y Diseño en Ingeniería, 11 (1995), pp. 383–400.

[15] C. Johnson, *Numerical Solution of Partial Differential Equations by the Finite Element Method*, Cambridge University Press, Cambridge-Lund, 1987.

[16] J. Kim and P. Moin, *Transport of passive scalars in a turbulent channel flow*, in Proceedings of the 6th Symposium on Turbulent Shear Flows, Toulise, France, 1987.

[17] S.L. Lyons, T.J. Hanratty, and J.B. McLaughlin, *Direct numerical simulation of passive heat transfer in a turbulent channel flow*, Int. J. Heat Mass Transfer, 34 (1991), pp. 1149–1161.

[18] M. Millán, M.J. Estrela, and V. Caselles, *Torrential precipitations on the Spanish East Coast: The role of the Mediterranean Sea surface temperature*, Atmos. Res., 36 (1995), pp. 1–16.

[19] R.D. Mills, *On the closed motion of fluid in a square cavity*, J. R. Aeronaut. Soc., 69 (1965), pp. 116–120.

[20] C. Nonino and S. Del Giudice, *Finite element analysis of turbulent forced convection in lid-driven rectangular cavities*, Internat. J. Numer. Methods Fluids, 25 (1988), pp. 313–329.

[21] O. Pironneau *On the transport-diffusion algorithm and its applications to the Navier-Stokes equations*, Numer. Math., (38 1982), pp. 309–332.

[22] B.G. Polyak, M. Fernández, M.D. Khutorskoy, J.I. Soto, I.A. Basov, M.C. Comas, V.Ye. Khain, B. Alonso, G.V. Agapova, I.S. Mazurova, A. Negredo, V.O. Tochitsky, J. de la Linde, N.A. Bogdanov, and E. Banda, *Heat flow in the Alboran Sea, Western Mediterranean*, Tectonophysics, 263 (1996), pp. 191–218.

[23] P. Sagaut, *Large Eddy Simulation for Incompressible Flows*, Springer, New York, 2001.

[24] M. Seaïd M and M. El-Amrani, *Lagrange-Galerkin method for unsteady free surface water waves*, Comput. Vis. Sci., 9 (2006), pp. 209–228.

[25] M. Seaïd, *On the quasi-monotone modified method of characteristics for transport-diffusion problems with reactive sources*, Comput. Methods Appl. Math., 2 (2002), pp. 186–210.

[26] M. Seaïd, *Semi-Lagrangian integration schemes for viscous incompressible flows*, Comput. Methods Appl. Math., 4 (2002), pp. 392–409.

[27] J.S. Smagorinsky, *General circulation experiments with the primitive equations*, Monthly Weather Rev., 91 (1963), pp. 99–164.

[28] A. Staniforth, and J. Côté, *Semi-Lagrangian integration schemes for the atmospheric models—A review*, Monthly Weather Rev., 119 (1991), pp. 2206–2223.

[29] E. Süli, *Convergence and nonlinear stability of the Lagrange-Galerkin method for the Navier-stokes equations*, Numer. Math., 53 (1988), pp. 1025–1039.

[30] C. Temperton and A. Staniforth, *An efficient two-time-level semi-Lagrangian semi-implicit integration scheme*, Q. J. Roy. Meteor. Soc., 113 (1987), pp. 1025–1039.

[31] R. Verfürth, *Error estimates for a mixed finite element approximation of the Stokes equation*, RAIRO Anal. Numer., 18 (1984), pp. 175–182.

[32] S. Zalesak, *Fully multidimensional flux-corrected transport algorithms for fluids*, J. Comput. Phys., 31 (1979), pp. 335–362.